RSC Advances

PAPER

Check for updates

Synthesis of a MnS/Ni$_x$S$_y$ composite with nanoparticles coated on hexagonal sheet structures as an advanced electrode material for asymmetric supercapacitors†

Qing Pan,‡[a] Xijia Yang,‡[b] Xiaohong Yang,[a] Lianfeng Duan[b] and Lijun Zhao ⓘD *[a]

Herein, a facile hydrothermal method was designed to synthesize a novel structure of micro-flowers decorated with nanoparticles. The micro-flower structure consists of enormous cross-linked flat hexagonal nanosheets with sufficient internal space, providing fluent ionic channels and enduring volume change in the electrochemical storage process. As expected, the MnS/Ni$_x$S$_y$ (NMS) electrode exhibits a relatively high specific capacitance of 1073.81 F g^{-1} (at 1 A g^{-1}) and a good cycling stability with 82.14% retention after 2500 cycles (at 10 A g^{-1}). Furthermore, the assembled asymmetric supercapacitor achieves a high energy density of 46.04 W h kg^{-1} (at a power density of 850 W kg^{-1}) and exhibits excellent cycling stability with 89.47% retention after 10 000 cycles. The remarkable electrochemical behavior corroborates that NMS can serve as an advanced electrode material.

1. Introduction

Driven by the growing demand for clean, renewable and uninterruptible energy supply as well as mobile power sources, the development of highly efficient energy conversion and storage devices has become a key challenge.[1] Supercapacitors (SCs), as newly emerging energy-storage devices, have attracted significant scientific interest due to their sustainable cycle life, high power density, and easy preparation process. These supercapacitors have been applied in various fields such as in hybrid electric vehicles, military devices, high-power electric devices and portable electronics.[2–8] However, the poor energy density (~5–20 W h kg^{-1}) and low potential window of electric double-layer capacitors (EDLCs) inhibit their large-scale practical application to a great degree.[9–11] An efficacious way to improve this situation is to utilize battery-type electrode materials, such as Ni(OH)$_2$, cobalt oxides, and sulfides, as the energy source.[11–13]

At present, metal oxides have drawn significant attention because the reversible faradaic reaction and multiple valence state changes endow them with higher theoretical capacity.[14–18] For example, Xia *et al.* successfully synthesized K$_x$MnO$_2$ and

Na$_{0.5}$MnO$_2$ electrodes for high-performance supercapacitors.[19,20] However, the surface redox reactions of the metal oxides are always retarded; this is because of the intrinsic poor electrical conductivity or the slow ion transport kinetics.[21] Contrary to transition metal oxides (such as NiO, Co$_3$O$_4$, MnO$_2$),[18,22–24] their sulfides present an enhanced electronic conductivity owing to their lower energy gap values.[25,26] Moreover, sulfur has a low electron negativity that endows it with more feasibilities of creating more flexible structures and thus prevents structure disintegration and ensures easier charge transportation.[27] Amongst all sulfur compounds, MnS is a promising candidate for potential application in energy storage devices due to the rich variable valence states of the Mn element as well as its low cost. To date, a number of studies have reported that binary Ni/Mn nanocomposites have achieved more superior capacitive performance than the monometallic sulfides due to the beneficial synergistic effect between Ni and Mn-based components. Zhao *et al.* successfully synthesized a NiMn-LDH/CNT architecture as an electrode with good electrochemical performance.[28] Wan *et al.* synthesized hedgehog-like hollow Ni–Mn oxides and sulfides by a one-step directional Mn-induced approach, and the capacitance improved about 26.35% after sulfuring.[29] Chen *et al.* reported a microflower-like Ni–Mn composite with nanosheet petals. After the sulfurization process, not only the capacitance improved, but also the cycling retention extended about 12% after 1500 cycles as compared to the case of the pristine NiMn-layered double hydroxides.[4]

Moreover, the design of functionalized microstructures plays a crucial role in improving the capacitance performance of nanohybrids. Extensive endeavors have been made to explore the

[a]Key Laboratory of Automobile Materials (Jilin University), Ministry of Education, College of Materials Science and Engineering, Nanling Campus, Changchun, 130025, P. R. China. E-mail: lijunzhao@jlu.edu.cn; Fax: +86-431-85095876

[b]Key Laboratory of Advanced Structural Materials, Ministry of Education, Department of Materials Science and Engineering, Changchun University of Technology, Changchun 130012, China

† Electronic supplementary information (ESI) available. See DOI: 10.1039/c8ra02063a

‡ These authors contributed equally to this work.

flower-like structures owing to their versatile merits of large specific surface area and abundant available internal space. In addition, previous studies have stated that ultrafine nanoparticles *in situ* grown on the nanosheets will not only significantly promote the specific surface area but also efficiently stimulate the synergistic effect owing to the robust incorporation of heterostructures. Pang *et al.* synthesized a heterogeneous Co_3O_4-nanocube/$Co(OH)_2$-nanosheet hybrid *via* a facial hydrothermal reaction.[30] Guan *et al.* designed $ZnMnO_4$ nanoparticles encapsulated in carbon sheets and employed them for supercapacitors.[31] Therefore, a distinct micro-flower structure decorated with nanoparticles has been successfully synthesized in our research.

Herein, the MnS/Ni_xS_y (NMS) composite with nanoparticles coated on hexagonal sheet structures has been successfully synthesized *via* a facial hydrothermal method. The suitable hexagonal sheet morphology with plenty of nanoparticles accelerated the electron transfer rate and ensured a fast and reversible faradaic reaction. When utilized for a supercapacitor electrode, NMS exhibited remarkable electric properties of a high specific capacitance (1073.81 F g^{-1} at 1 A g^{-1}) and elevated cycling retention (82.14% retention after 2500 cycles). Furthermore, an asymmetric supercapacitor (based on positive NMS and negative AC electrodes) was fabricated, which also displayed an excellent performance with long-term cycling duration and a high energy density (46.04 W h kg^{-1} at a power density of 0.85 kW kg^{-1}). All these properties corroborate the high feasibility of NMS for application in the energy-storage field.

2. Experimental

2.1 Preparation of the Ni–Mn precursor

The Ni–Mn precursor was synthesized by a facile hydrothermal method. In a typical process, 1.5 mmol of manganese chloride tetrahydrate ($MnCl_2 \cdot 4H_2O$), 3 mmol of nickel chloride hexahydrate ($NiCl_2 \cdot 6H_2O$), and 12 mmol of urea were dissolved in 75 mL of deionized water under magnetic stirring for 30 minutes. Subsequently, the as-prepared solution was transferred to a 100 mL Teflon-lined autoclave, which was heated at an oven temperature of 120 °C for 6 h to obtain the Ni–Mn precursor. The synthesized precursor powder was centrifuged at 8500 rpm, rinsed with deionized water and absolute ethanol, and vacuum dried at 60 °C overnight.

2.2 Preparation of the NMS composite

Typically, 20 mL of $Na_2S \cdot 9H_2O$ (360 mg) aqueous solution was poured into 20 mL of Ni–Mn precursor (100 mg) aqueous solution under magnetic stirring until the solution became black. The black suspension was transferred into a 50 mL Teflon-lined autoclave, which was kept at 100 °C for 6 h. In the end, the resultant powder was thoroughly centrifuged, washed with deionized water and absolute ethanol, and freeze-dried for further use. The synthesized sample was named as NMS. Similarly, we also adjusted the concentration of the precursor solution (1.5 mmol of $NiCl_2 \cdot 6H_2O$ and 3 mmol $MnCl_2 \cdot 4H_2O$, as well as 3 mmol of $NiCl_2 \cdot 6H_2O$ and 3 mmol $MnCl_2 \cdot 4H_2O$), and the other conditions were kept unchanged; the as-synthesized

powders were named as NMS-1 and NMS-2. For comparison, MS and NS were also synthesized *via* the same process without the introduction of Ni^{2+} or Mn^{2+}.

2.3 Material characterization

A field emission scanning electron microscope (FE-SEM, JSM-6700F) and high-resolution TEM (HRTEM) were applied to study the morphologies and size of the as-prepared samples. The XRD spectra of the sample were characterized by powder X-ray diffraction (XRD, Rigaku D/MAX 2500PC). X-ray photoelectron spectroscopy (XPS) was conducted to investigate the electronic states *via* an ESCALAB MkII (Vacuum generators) spectrometer with Al Kα X-ray (240 W).

2.4 Electrode preparation and electrochemical measurements

The NMS composite, acetylene black, and polyvinylidene difluoride (PVDF) were mixed in a ratio of 80 : 15 : 5 by weight with *N*-methyl-2-pyrrolidone (NMP) to form the coating paste. The paste was then applied to nickel foam (the spread area was about 10 mm × 10 mm), which was then dried at 80 °C for 8 h in vacuum. The loading density of the active materials was about 1.5–2.0 mg cm^{-2}. To fabricate the asymmetric supercapacitor, a negative electrode was also prepared, for which AC and polytetrafluoroethylene (as a binder) were mixed in a weight ratio of 9 : 1, and then, the mixture was applied to a 10 mm × 10 mm Ni foam under a pressure of 10 MPa for 30 s.

An electrochemical working station (CHI660e, Shanghai, China) was used to perform the electrochemical experiments. The NMS composite electrode was utilized as a working electrode; the platinum counter electrode and the saturated calomel electrode (SCE) reference electrodes were placed in a 3 M KOH aqueous electrolyte.

2.5 Calculations

The specific capacitance of the single electrode and assembly device can be easily calculated by the following equation:

$$C_s = I\Delta t/(m\Delta V) \tag{1}$$

where C_s represents the specific capacitance and is expressed as F g^{-1}, and I (A), Δt (s), m (g) and ΔV (V) stand for the discharge current, discharge time, voltage change and the total mass of the active materials on the single electrode or in the individual device, respectively.

The most optimal mass ratio of the NMS positive electrode and AC negative electrode can be easily calculated referring to eqn (2) as follows:

$$m^+/m^- = C_s^- \, \Delta V^-/(C_s^+ \Delta V^+) \tag{2}$$

where m (g), C_s (F g^{-1}) and ΔV (V) stand for the mass of active materials, specific capacitance and discharge voltage, respectively.

The energy density (E) and power density (P) for the two-electrode devices can be calculated using the following formulae:

$$E = 0.5C_s \, V^2 \tag{3}$$

$$P = E/\Delta t \tag{4}$$

where C_s (F g^{-1}), ΔV (V), Δt (s), E (W h kg^{-1}) and P (W kg^{-1}) stand for the specific capacitance, voltage range, discharge time, energy density and the power density of the assembled supercapacitor device, respectively.

3. Result and discussion

3.1 Structure and morphology of the NMS composite

The morphological details of the NMS composite were examined using FESEM. Fig. 1a shows the novel NMS morphology of the nanoparticles coated on the 3D micro-flower structure; these micro-flowers display a diameter of *ca.* 2–3 μm and thickness of *ca.* 70 nm. Moreover, the flat internal microsheets and open porous characteristics provide more active sites for the diffusion reaction between the NMS composite and KOH electrolyte. Conversely, the absence of either Ni or Mn will cause agglomeration of the system as well as lead to different structures (Fig. S1a and b†). Therefore, we adjusted the molar ratio of Ni/Mn salts to further control the morphology and highlight the superiority of the NMS composite. As displayed in Fig. S1c,†

when the molar ratio of Ni/Mn was 1 : 2, the sheet-like structure became smaller, whereas the number of nanoparticles increased. In Fig. S1d,† these samples display thinner and smaller sheets with the absence of nanoparticles. Hence, we expected that NMS with heterogeneous structures would show higher electrochemical performance.

To further investigate the morphology of NMS, TEM and HRTEM measurements were performed. Fig. 1b revealed that the hierarchical nanosheets vertically expanded outward along the normal direction. The dark area in the TEM image results from the overlap of the multi-sheet structure. In the HRTEM image shown in Fig. 1c, the lattice fringe spacings of 0.17 and 0.29 nm separately correspond to the (401) and (101) planes of NiS, whereas the distances 0.34, 0.31, 0.18, 0.20, and 0.17 nm conform to the (100), (101), (103), (110), and (112) planes of MnS, respectively. In addition, the distribution of MnS fringes is close to a circle (as marked by the yellow circle in Fig. 1c), whereas NiS is distributed widely and continuously; thus, there is a great possibility that the particles are MnS, and the hexagonal sheets are NiS. In addition, the chemical content of NMS is accurately evaluated *via* EDX measurement, as depicted in Fig. S2,† powerfully demonstrating the existence of Ni, Mn and S elements. In the EDX measurement, we used the copper network as a substrate. Thus, apart from the three elements Ni, Mn, and S, the Cu peak can also be detected. Moreover, the elemental distribution of NMS in Fig. 1d–f reveals uniform distribution of these elements.
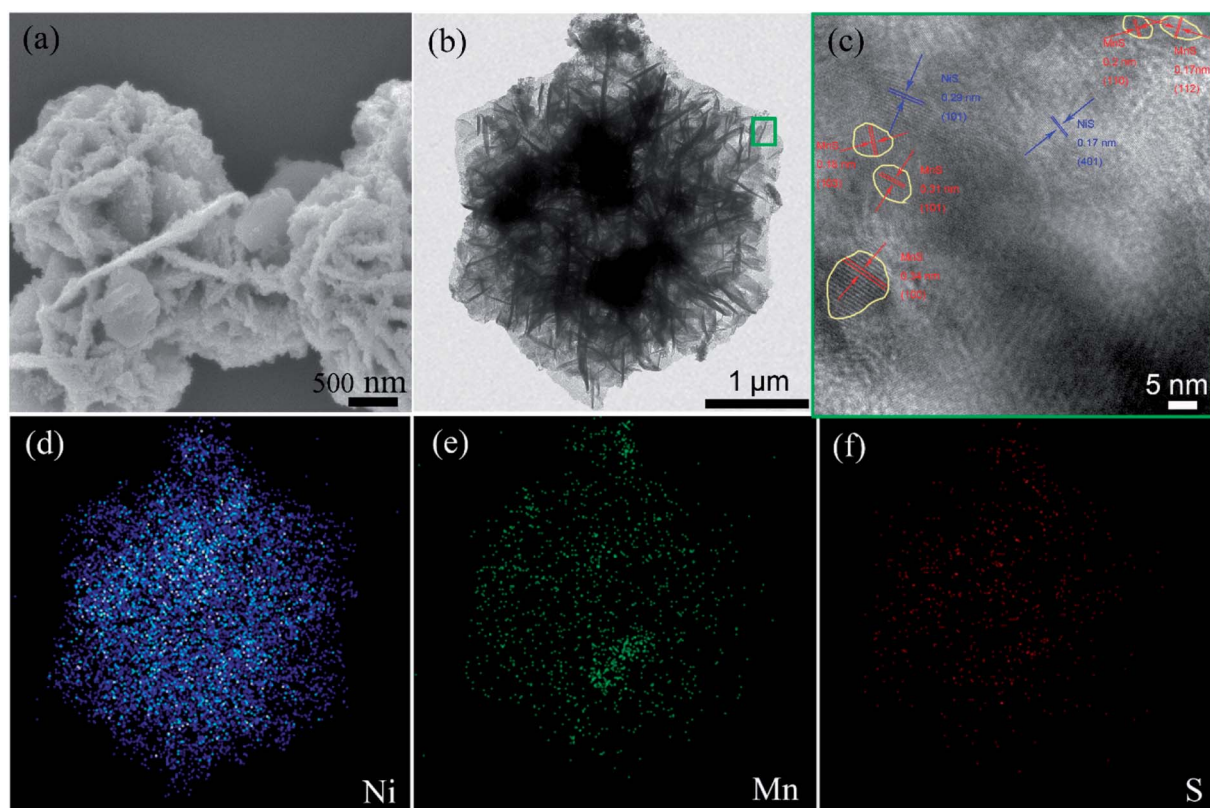

Fig. 1 (a) FE-SEM; (b) TEM image of the as-prepared NMS; (c) HRTEM image of the green square in "(b)"; the elemental mapping of the NMS composite in (b): (d) Ni, (e) Mn and (f) S element.

The as-prepared NMS composite was further tested through XRD patterns, as provided in Fig. 2a. The peaks at 25.8°, 27.6°, 29.3°, 38.2°, 45.6°, 49.9°, 54.1° and 55.1° separately correspond to the (100), (002), (101), (102), (110), (103), (201) and (112) planes of the MnS phase (JCPDS card no. 65-3413).[32] The peaks at 18.7°, 30.4°, 37.9° and 40.8° are attributed to the (110), (101), (220) and (211) planes of the NiS phase (JCPDS card no.02-1208),[33,34] respectively. Some other diffraction peaks, as shown in Fig. 2a, may result from nickel sulfides (NiS_2 phase (JCPDS card no. 65-3325)[35] and Ni_7S_6 phase (JCPDS card no. 54-0931)).[36] The XRD patterns of the Ni–Mn precursor and other sulfides are also shown. As shown in Fig. S3b,† the diffraction peaks of the Ni–Mn precursor can be reasonably indexed to a series of crystal planes, demonstrating successful preparation of NiMn hydroxide,[4,28] whereas the MS samples are MnS/MnS_2 composites, and NS is mainly attributed to the Ni_7S_6 phase (Fig. S3a†).

Furthermore, the chemical composition and metal states of the NMS composite were detected by XPS measurement. In the Mn 2p spectrum shown in Fig. 2b, two major peaks at 653.75 eV and 641.75 eV are separately attributed to the Mn $2p_{1/2}$ and $2p_{3/2}$ levels, wherein the Mn $2p_{3/2}$ characteristic peak reveals the presence of Mn ions in the divalent state.[37] The Ni 2p spectrum

(Fig. 2c) can be best fitted with two spin–orbit doublets and two shakeup satellites *via* the Gaussian fitting method. The doublets at 853.5 and 870.7 eV separately correspond to the binding energies of Ni $2p_{3/2}$ and $2p_{1/2}$ levels, representing the typical binding energies of Ni^{2+}.[16] However, the peaks at 855.8 and 873.7 eV are respectively attributed to the $2p_{3/2}$ and $2p_{1/2}$ levels of Ni^{3+}.[38,39] As clearly shown in Fig. 2d, the detailed spectrum of S 2p shows two peaks of S $2p_{1/2}$ and $2p_{3/2}$ at 162.8 and 161.65 eV, respectively, as well as a concomitant shake-up satellite peak.[39,40] Therefore, the XPS spectra further coincide well with the multi-phase composition of NMS, composed of various nickel sulfides and MnS phases. Interestingly, the pronounced divergence about the valence state of the Ni element is displayed in the XRD and XPS pattern. Thus, we generally denoted these various nickel sulfides as Ni_xS_y.

To shed light on the growth progress of this novel NMS structure, we further explored the samples (obtained at different sulfurization stages) *via* the FE-SEM techniques (Fig. 3), and the corresponding XRD patterns are shown in Fig. S3b.† Fig. 3a shows the FE-SEM image of blurry flowery Ni–Mn precursor. After sulfurization for 0.5 h (Fig. 3b), the blurry Ni–Mn precursor becomes smooth, and a large thick piece begins to
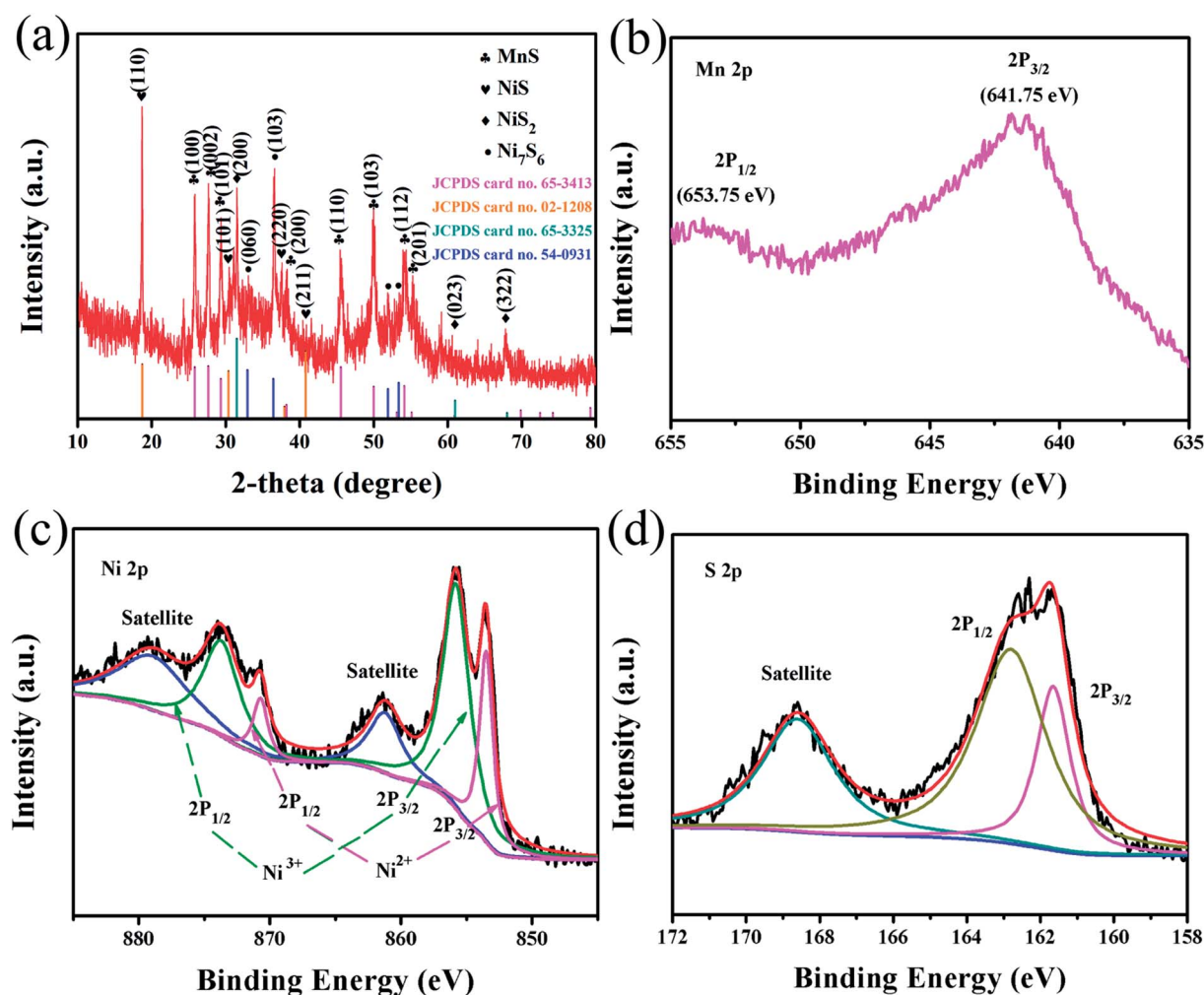

Fig. 2   (a) XRD pattern of the as-prepared NMS; XPS spectra of the NMS: (b) Mn 2p peaks, (c) Ni 2p peaks, and (d) S 2p peaks.
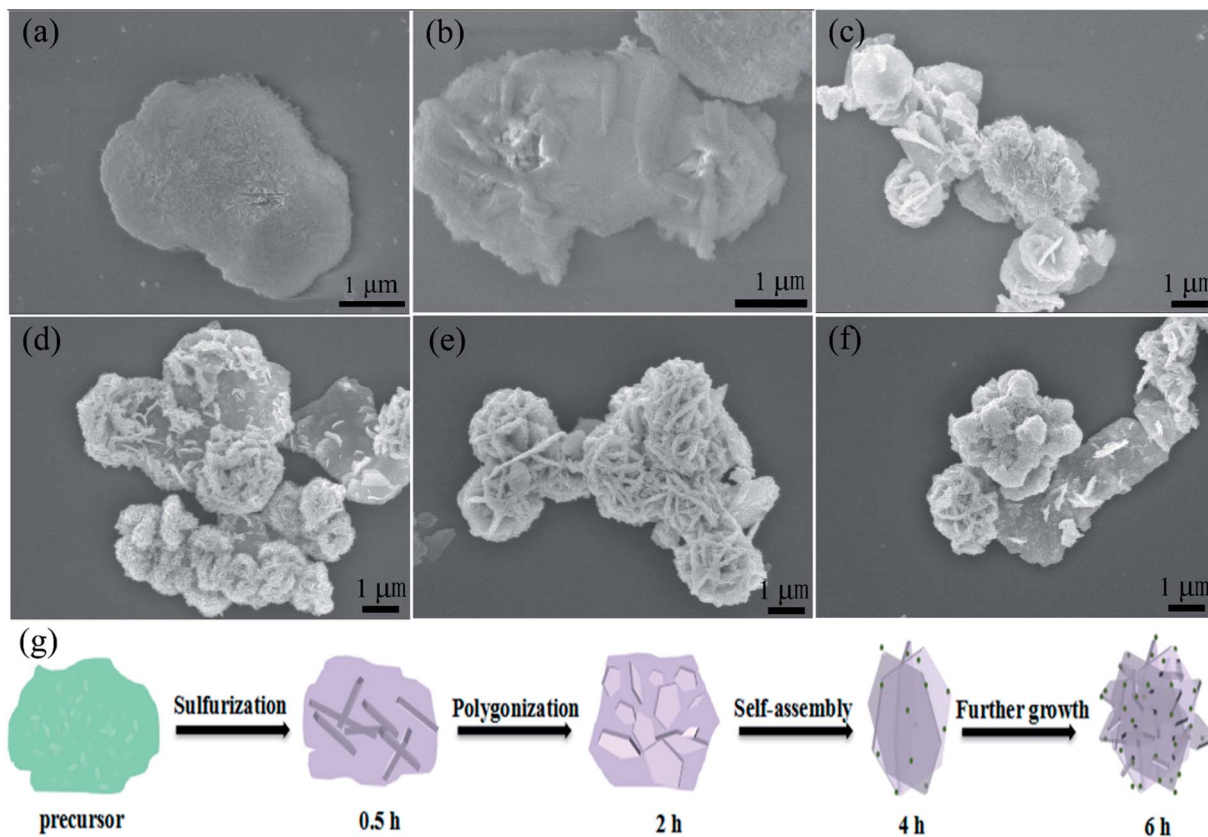
Fig. 3 FE-SEM image of the (a) Ni–Mn precursor; the Ni–Mn precursor with different sulfurization times: (b) 0.5, (c) 2, (d) 4, (e) 6 and (f) 8 h; (g) schematic of the morphology changes from the precursor to NMS.
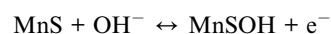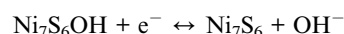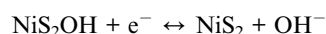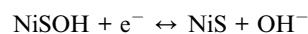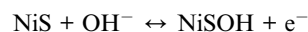
regenerate. As shown in Fig. S3b,† some Ni_xS_y diffraction peaks can be observed. After sulfurization treatment for 2 h, hexagonal sheets gradually regenerate with a thicker size, as depicted in Fig. 3c. In the stage of 4 h (Fig. 3d), the hexagonal sheets gather and self-assemble to form a micro-flower structure, which exhibit an obvious decrease in thickness. After 6 h (Fig. 3e), NMS was obtained, possessing uniform morphology with a covering of nanoparticles. Compared to the case of the samples obtained after sulfurization for 2 h or 4 h, stronger MnS peaks can be detected in NMS. However, as shown in Fig. 3f, excess sulfurization time (8 h) would result in obvious enrichment of nanoparticles and increase the thickness of microsheets.

On the basis of the abovementioned FE-SEM description and the corresponding XRD results, the growth progress of the NMS structures is probably as follows (Fig. 3g): (1) in the beginning, S ion formed by $Na_2S·9H_2O$ reacts with the Ni–Mn precursor; then, the product aggregates to cause nucleation; (2) after nucleation, the nucleation center grows into hexagonal sheets; (3) then, the hexagonal sheets self-assemble with the nanoparticles coated on them; and (4) after further growth, the NMS novel structure is finally built.

3.2 Electrochemical performance of the NMS electrodes

A three-electrode test system was employed to further evaluate the energy-storage capacitance of MS, NS, NMS, NMS-1 and NMS-2 electrodes. Fig. 4a shows comparison of the different CV curves of these electrodes at a scan rate of 5 mV s^{-1}. Amongst them, NMS showed larger integrated area with stronger redox peaks, suggesting its superior capacitance behavior. A series of typical anodic and cathodic peaks are visible in these CV curves, which show significant difference in comparison with the ideal rectangular CV curves of EDLCs.[5,10] Then, the detailed CV curves of the NMS electrode are shown in Fig. 4b at different scan rates ranging from 5 to 100 mV s^{-1}. With the increasing scan rates, the initial shapes could be generally maintained, but the anodic peak shifted positively and the cathodic peak shifted negatively; this was due to the increased diffusion resistance and electrode polarization.[41,42] The faradaic reactions corresponding to the redox peaks are as follows:

$$NiS + OH^- \leftrightarrow NiSOH + e^-$$

$$NiSOH + e^- \leftrightarrow NiS + OH^-$$

$$NiS_2 + OH^- \leftrightarrow NiS_2OH + e^-$$

$$NiS_2OH + e^- \leftrightarrow NiS_2 + OH^-$$

$$Ni_7S_6 + OH^- \leftrightarrow Ni_7S_6OH + e^-$$

$$Ni_7S_6OH + e^- \leftrightarrow Ni_7S_6 + OH^-$$

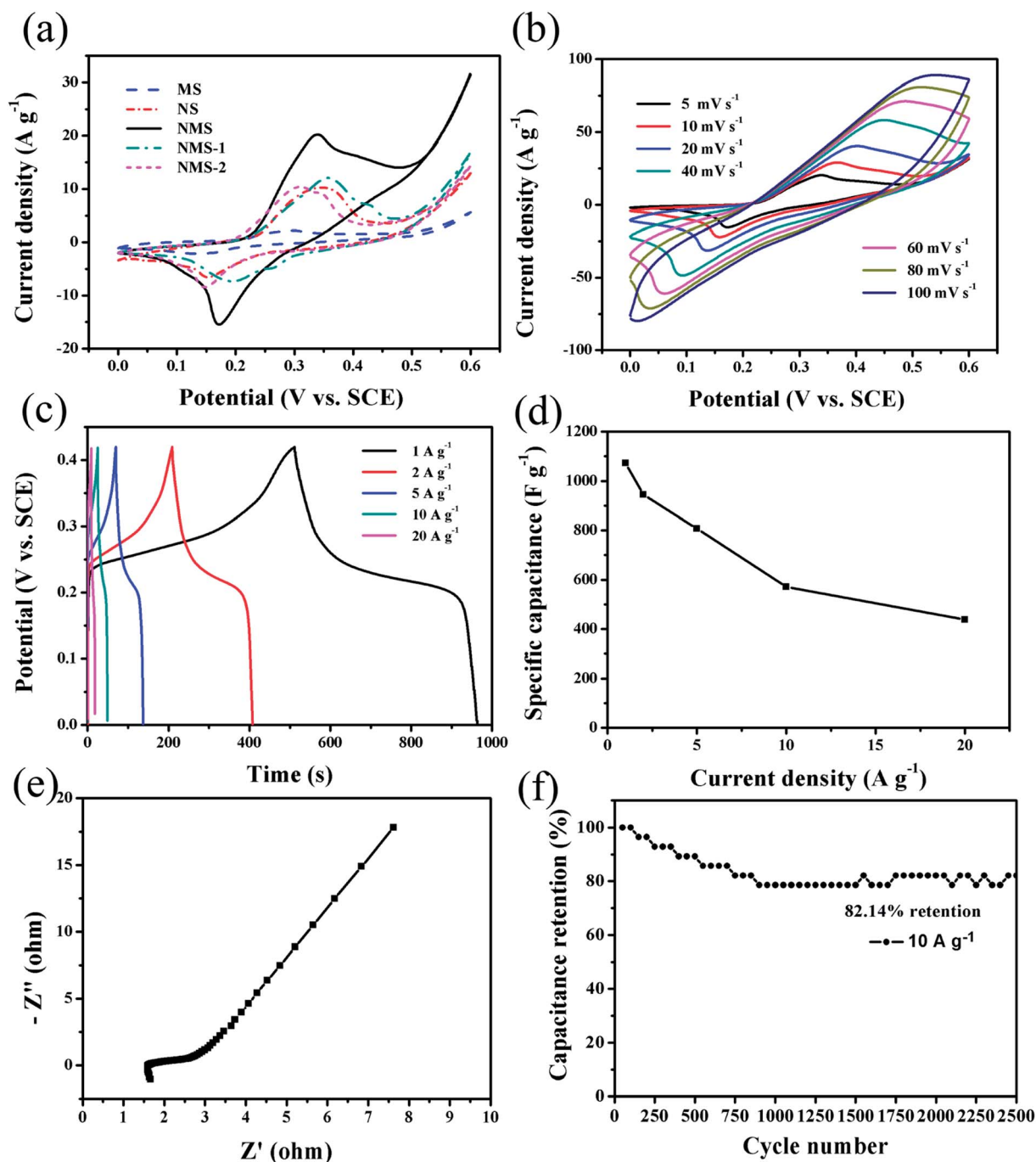$$MnS + OH^- \leftrightarrow MnSOH + e^-$$

Fig. 4 (a) Comparison of the CV curves of typical MS, NS, NMS, NMS-1 and NMS-2 electrodes at a scan rate of 5 mV s^{-1}; (b) CV curves of NMS electrodes at different scan rates; (c) galvanostatic charge–discharge curves of the NMS electrode at different current density; (d) C_s of the NMS electrode; (e) Nyquist plots of the NMS electrodes; (f) cycling performance at 10 A g^{-1} of the NMS electrode.

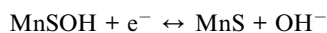$$MnSOH + e^- \leftrightarrow MnS + OH^-$$

Fig. 4c shows the GCD characteristics of the as-prepared NMS electrode in the potential range of 0–0.42 V. The specific capacitance at various discharge current densities can be calculated *via* eqn (1) and are displayed in Fig. 4d. The obtained specific capacitance values of the NMS electrode are 1073.81, 944.76, 807.14, 571.43 and 428.57 F g^{-1} at the current densities of 1, 2, 5, 10, and 20 A g^{-1}, respectively. For comparison, the

electrochemical performances of MS, NS, NMS-1, and NMS-2 were also evaluated at a current density of 1 A g^{-1} (Fig. 5a and b). Compared with MS, NS, NMS-1, and NMS-2 electrodes, NMS presented an improved specific capacitance. The good electrochemical properties of NMS can be attributed to the synergistic effect of MnS and Ni$_x$S$_y$: (1) the hybrid manganese sulfide and nickel sulfide undergo redox reactions, which result in enhanced specific capacitances; (2) the stable 3D micro-flowers are constructed by the 2D hexagonal sheets, increasing the

specific surface area and shortening the diffusion route to a great extent, benefiting both ion and electron transfer during the charge–discharge process; (3) the micro-flower structure can endure volume change in the electrochemical storage process; and (4) nanoparticles directly growing on the 3D networked micro-flowers not only provide more electrochemical active sites for redox reactions, but are also beneficial for the contact with the electrolyte. Hence, the NMS electrode performed best amongst all our materials.

The EIS measurements of NMS were carried out to further analyze the resistances of these electrodes. In the Nyquist plots of Fig. 4e and 5c, Z' and Z'' represent the real and imaginary parts of the impedance, respectively.[43,44] The intersection of x-axis at a high frequency demonstrates the equivalent series resistance (ESR), which reveals multiple resistances including the intrinsic resistance of the active materials, electrolytic resistance, and the contact resistance between the electrolyte and active material. The ESR values of the MS, NS, NMS, NMS-1 and NMS-2 electrodes are 2.667, 1.668 1.66, 2.956 and 2.365 Ω, respectively. Moreover, contrary to other electrodes, NMS exhibited a smaller semicircle diameter and steeper straight line in high-frequency area; this verified low charge transfer resistance (R_{CT}) and diffusion resistance (Z_w). Therefore, the formation of binary metal sulfurization

compounds and the optimization of mole ratio could serve as an efficient strategy to significantly reduce the resistances, then cause a synergistic effect among different components, and finally promote the electrochemical performance.

The long-term cycling stability is always considered as a critical factor for extensive applications in energy-storage devices. In Fig. 4f, the capacitance retention of NMS dramatically attenuated during the initial 800 cycles and tended to stably decrease in the latter cycling measurement. Moreover, 82.14% retention was observed after 2500 cycles at 10 A g^{-1}, which was superior than those reported in previous studies and that of our other electrodes.[4,45] The improved supercapacitor property of the NMS electrode benefited from the distinct 3D cross-linked flowery structure with ultrafine nanoparticles on a great scale.[46] During the GCD processes, this 3D architecture has the self-adaptive strain-relaxation capability for more stable structures, thus leading to an improved cycle life.[43,47] Furthermore, the MnS nanoparticles directly coated onto the Ni$_x$S$_y$ nanosheets construct a heterostructure to shorten the diffusion length, which are greatly beneficial for the high-rate charge/discharge process, thus leading to the good electrochemical performance.[48] In addition, as shown in Fig. 5d, great discreteness from other comparisons was presented in long-
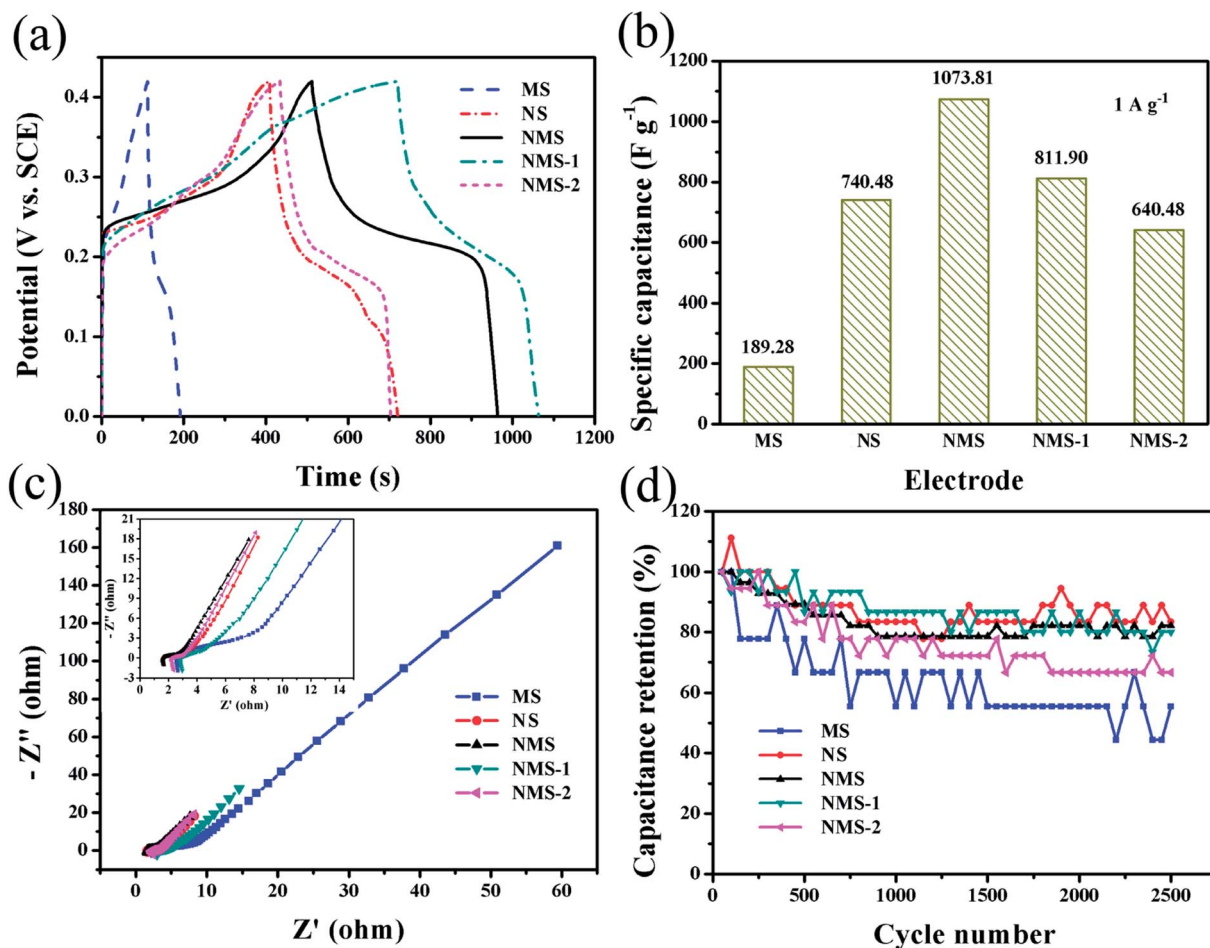

Fig. 5 (a) Charge−discharge curves and (b) the calculated specific capacitance of the MS, NS, NMS, NMS-1 and NMS-2 electrode; (c) Nyquist plots of the MS, NS, NMS, NMS-1 and NMS-2 electrode; and (d) cycling performance MS, NS, NMS, NMS-1 and NMS-2.

term cycling curves, which originated from the lower discharge time causing extremely fluctuant capacitance retention.

3.3 Asymmetric supercapacitor characterization

To further study the electrochemical property of the NMS electrode, we have further fabricated an asymmetric supercapacitor (NMS//AC, composed of positive NMS and negative AC electrodes), as exhibited in Fig. 6a. We fabricated the two-electrode asymmetric supercapacitor following the eqn (2), and the mass ratio of NMS to AC was about 1.73. Furthermore, the corresponding electrochemical test results are shown in Fig. S4.† The CV curves of the NMS//AC device (in Fig. 6b) exhibit a nearly rectangular shape, implying that there is a good charge matching between the positive and negative electrodes.
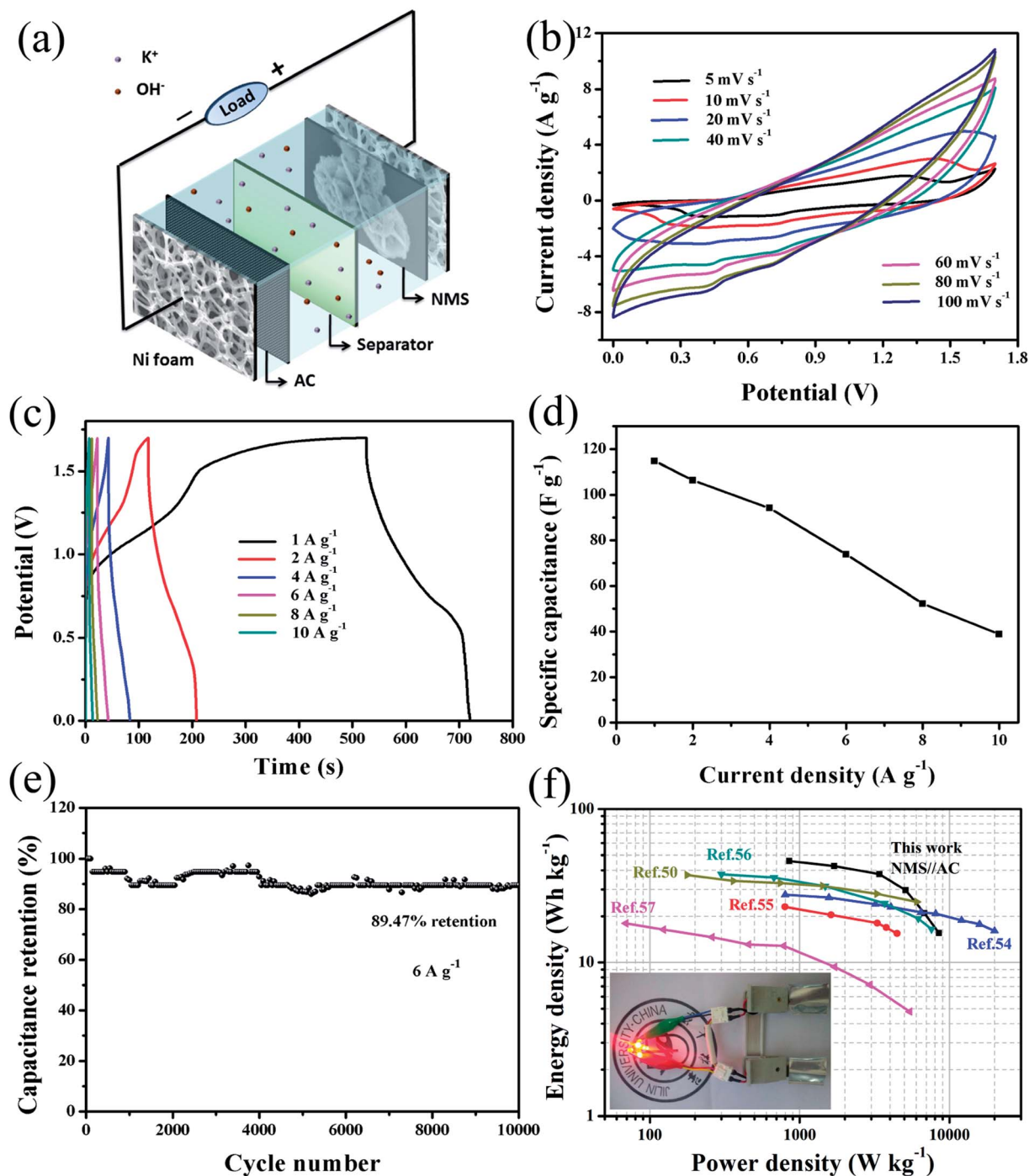

Fig. 6 (a) Structure schematic of the asymmetric supercapacitor device; (b) CV curves at various scanning rates; (c) galvanostatic charge–discharge curves; (d) the corresponding specific capacitance; (e) cycling performance at a current density of 6 A g^{-1}; (f) a Ragone plot between energy densities and power densities among our device and other references. The inset shows an image exhibiting that two NMS//AC supercapacitors in series can light up four red LED indicators.

Table 1 Comparisons of the specific capacity/capacitance, energy density and cycling stability based on NMS in the present study and other reported studies

Electrode material	Specific capacity/capacitance	Energy density	Cycling stability	Reference
NMS	1073.81 F g^{-1} at 1 A g^{-1}	46.04 W h kg^{-1} at 850 W kg^{-1}	89.47% 10 000 cycles 6 A g^{-1}	This work
Ni–Mn LDH nanosheets	881 F g^{-1} at 0.5 A g^{-1}	46.3 W h kg^{-1} at 112.6 W kg^{-1}	89% 6000 cycles 5 A g^{-1}	49
γ-MnS	573.9 F g^{-1} at 0.5 A g^{-1}	37.6 W h kg^{-1} at 181.2 W kg^{-1}	89.87% 5000 cycles 1 A g^{-1}	50
(Mn–Co) oxysulfide on Ni foam	490C g^{-1} (capacity) at 2 A g^{-1}	—	86.5% 3000 cycles 20 A g^{-1} (three-electrode system)	10
Co$_{2.5}$Mn$_{0.5}$ sulfide	289C g^{-1} at 1 A g^{-1}	22.3 W h kg^{-1} at 750 W kg^{-1}	85% 5000 cycles 3 A g^{-1}	11
Mn/Zn-BMO	251 F g^{-1} at 0.5 A g^{-1}	33.1 W h kg^{-1} at 4416 W kg^{-1}	99.6% 5000 cycles/—	51
Zn$_{0.25}$Mn$_{0.75}$S hollow spheres	664 F g^{-1} at 1 A g^{-1}	—	—	52
MnS/GO-NH$_3$	390.8 F g^{-1} at 0.25 A g^{-1}	14.9 W h kg^{-1} at 66.5 W kg^{-1}	81% 2000 cycles/—	53

The corresponding GCD curves were obtained (Fig. 6c) at various current densities in a wide potential window between 0 and 1.7 V. At a current density of 1 A g^{-1}, the capacitance for the device can reach as high as 114.71 F g^{-1}. On the other hand, the capacitance diminished with an increase in the current densities due to the incomplete charge–discharge process and electrode polarization at high current densities. However, the device still kept a value of 38.83 F g^{-1} at a high current density of 10 A g^{-1} (as shown in Fig. 6d).

The cycling duration of NMS//AC was also investigated. As presented in Fig. 6e, the specific capacitance decreased in the initial 2050 cycles and then generated a slight rebound (2100–3950 cycles); this might be attributed to electrode activation. After this, the capacitance remained relatively stable and achieved a higher retention of 89.47%, enduring 10 000 cycles. Furthermore, the Ragone plots for NMS//AC and other references are shown in Fig. 6f. According to the eqn (3) and (4), our NMS//AC asymmetric supercapacitor revealed a high energy density of 46.04 W h kg^{-1} at a power density of 0.85 kW kg^{-1}, which was superior to that of Mn- and Ni/Mn-based asymmetric supercapacitors such as γ-MnS/rGO-60//rGO,[54] α-MnS/N-rGO hybrid//N-rGO,[55] AC//LNC,[56] MnS//EDAC[50] and M-MCNF-based full cell supercapacitor.[57] The high specific capacitance (114.71 F g^{-1}) and large cell voltage (1.7 V) lead to the high energy density. In addition, as presented in Table 1, we also compared other important parameters with those of other related asymmetric supercapacitors to highlight the advantages of our device. Finally, two NMS//AC asymmetric supercapacitors were further assembled in series to intuitively display their practical application, which could effortlessly light up four red light-emitting diodes (LED) (1.8 V, 20 mA) (as shown in the inset of Fig. 6f). These impressive results powerfully testify the enormous potential of NMS for applications in energy storage.

4.   Conclusion

In our study, we have successfully fabricated an NMS electrode through a facile hydrothermal approach and subsequent sulfurization treatment. A novel flowery structure composed of flat hexagonal nanosheets and ultrafine nanoparticles endowed MNS with sufficient active areas for the diffusion reaction. The synergistic effect was due to the heterojunction between Ni$_x$S$_y$ and MnS at a bigger scale, promoting the diffusion of ions on the surface of the electrode; thus, NMS endured the change in volume in the long-term cycling process. Therefore, the as-synthesized NMS electrode can reach a high specific capacitance with favorable cycling stability. Moreover, we have further fabricated an NMS//AC asymmetric supercapacitor, which delivers a high specific energy density as well as an excellent cycling stability. In addition, two NMS//AC device in series could easily trigger the LED indicator, indicating potential for practical application.

Conflicts of interest

There are no conflicts to declare.

Acknowledgements

References

1 E. Mourad, L. Coustan, P. Lannelongue, D. Zigah, A. Mehdi, A. Vioux, S. A. Freunberger, F. Favier and O. Fontaine, *Nat. Mater.*, 2017, **16**, 446–453.

2 X. Liu, Z. Wu and Y. Yin, *Chem. Eng. J.*, 2017, **323**, 330–339.

3 L. Q. Mai, F. Yang, Y. L. Zhao, X. Xu, L. Xu and Y. Z. Luo, *Nat. Commun.*, 2011, **2**, 381.

4 J. Chen, X. Wang, J. Wang and P. S. Lee, *Adv. Energy Mater.*, 2016, **6**, 1501745.

5 G. Wang, L. Zhang and J. Zhang, *Chem. Soc. Rev.*, 2012, **41**, 797–828.

6 L. Wu, L. Hao, B. Pang, G. Wang, Y. Zhang and X. Li, *J. Mater. Chem. A*, 2017, **5**, 4629–4637.

7 Y. Zhao, L. Hu, S. Zhao and L. Wu, *Adv. Funct. Mater.*, 2016, **26**, 4085–4093.

8 R. R. Salunkhe, J. Lin, V. Malgras, S. X. Dou, J. H. Kim and Y. Yamauchi, *Nano Energy*, 2015, **11**, 211–218.

9 J. Jiang, Y. Li, J. Liu, X. Huang, C. Yuan and X. W. Lou, *Adv. Mater.*, 2012, **24**, 5166–5180.

10 M. Liu, Y. Fu, H. Ma, T. Wang, C. Guan and K. Hu, *Electrochim. Acta*, 2016, **191**, 916–922.

11 S. Chen, H. Chen, C. Li, M. Fan, C. Lv, G. Tian and K. Shu, *J. Mater. Sci.*, 2017, **52**, 6687–6696.

12 P. Simon, Y. Gogotsi and B. Dunn, *Science*, 2014, **343**, 1210–1211.

13 T. Brousse, D. Belanger and J. W. Long, *J. Electrochem. Soc.*, 2015, **162**, A5185–A5189.

14 H. Tang, J. Wang, H. Yin, H. Zhao, D. Wang and Z. Tang, *Adv. Mater.*, 2015, **27**, 1117–1123.

15 G. He, J. Li, W. Li, B. Li, N. Noor, K. Xu, J. Hu and I. P. Parkin, *J. Mater. Chem. A*, 2015, **3**, 14272–14278.

16 J. Yang, C. Yu, X. Fan, S. Liang, S. Li, H. Huang, Z. Ling, C. Hao and J. Qiu, *Energy Environ. Sci.*, 2016, **9**, 1299–1307.

17 V. Augustyn, P. Simon and B. Dunn, *Energy Environ. Sci.*, 2014, **7**, 1597.

18 S. Zhu, L. Li, J. Liu, H. Wang, T. Wang, Y. Zhang, L. Zhang, R. S. Ruoff and F. Dong, *ACS Nano*, 2018, **12**, 1033–1042.

19 N. Jabeen, A. Hussain, Q. Xia, S. Sun, J. Zhu and H. Xia, *Adv. Mater.*, 2017, **29**, 1700804.

20 N. Jabeen, Q. Xia, S. V. Savilov, S. M. Aldoshin, Y. Yu and H. Xia, *ACS Appl. Mater. Interfaces*, 2016, **8**, 33732–33740.

21 L. Liu, *Nanoscale*, 2013, **5**, 11615–11619.

22 Y. Lu, L. Yu, M. Wu, Y. Wang and X. W. D. Lou, *Adv. Mater.*, 2018, **30**, 12464–12472.

23 J. Liu, J. Jiang, C. Cheng, H. Li, J. Zhang, H. Gong and H. J. Fan, *Adv. Mater.*, 2011, **23**, 2076–2081.

24 Y. Ouyang, X. Xia, H. Ye, L. Wang, X. Jiao, W. Lei and Q. Hao, *ACS Appl. Mater. Interfaces*, 2018, **10**, 3549–3561.

25 M. S. Javed, X. Han, C. Hu, M. Zhou, Z. Huang, X. Tang and X. Gu, *ACS Appl. Mater. Interfaces*, 2016, **8**, 24621–24628.

26 Y. Tang, S. Chen, S. Mu, T. Chen, Y. Qiao, S. Yu and F. Gao, *ACS Appl. Mater. Interfaces*, 2016, **8**, 9721–9732.

27 Z. Zeng, D. Wang, J. Zhu, F. Xiao, Y. Li and X. Zhu, *CrystEngComm*, 2016, **18**, 2363–2374.

28 J. Zhao, J. Chen, S. Xu, M. Shao, Q. Zhang, F. Wei, J. Ma, M. Wei, D. G. Evans and X. Duan, *Adv. Funct. Mater.*, 2014, **24**, 2938–2946.

29 H. Wan, J. Jiang, Y. Ruan, J. Yu, L. Zhang, H. Chen, L. Miao and S. Bie, *Part. Part. Syst. Charact.*, 2014, **31**, 857–862.

30 H. Pang, X. Li, Q. Zhao, H. Xue, W.-Y. Lai, Z. Hu and W. Huang, *Nano Energy*, 2017, **35**, 138–145.

31 Y. Guan, Y. Feng, Y. Mu, L. Fang, H. Zhang and Y. Wang, *Nanotechnology*, 2016, **27**, 475402.

32 X. Li, J. Shen, N. Li and M. Ye, *J. Power Sources*, 2015, **282**, 194–201.

33 B. Guan, Y. Li, B. Yin, K. Liu, D. Wang, H. Zhang and C. Cheng, *Chem. Eng. J.*, 2017, **308**, 1165–1173.

34 X. Yang, L. Zhao and J. Lian, *J. Power Sources*, 2017, **343**, 373–382.

35 Z. Dai, X. Zang, J. Yang, C. Sun, W. Si, W. Huang and X. Dong, *ACS Appl. Mater. Interfaces*, 2015, **7**, 25396–25401.

36 Z. Li, J. Han, L. Fan and R. Guo, *CrystEngComm*, 2015, **17**, 1952–1958.

37 J. Tang, J. Shen, N. Li and M. Ye, *J. Alloys Compd.*, 2016, **666**, 15–22.

38 C. Lamiel, V. H. Nguyen, D. R. Kumar and J.-J. Shim, *Chem. Eng. J.*, 2017, **316**, 1091–1102.

39 Z. Zhang, Q. Wang, C. Zhao, S. Min and X. Qian, *ACS Appl. Mater. Interfaces*, 2015, **7**, 4861–4868.

40 Y. Ruan, J. Jiang, H. Wan, X. Ji, L. Miao, L. Peng, B. Zhang, L. Lv and J. Liu, *J. Power Sources*, 2016, **301**, 122–130.

41 J. Ji, L. Zhang, H. Ji, Y. Li, X. Zhao, X. Bai, X. Fan, F. Zhang and R. Ruoff, *ACS Nano*, 2013, **7**, 6237–6243.

42 J. Liu, J. Wang, Z. Ku, H. Wang, S. Chen, L. Zhang, J. Lin and Z. X. Shen, *ACS Nano*, 2016, **10**, 1007–1016.

43 X. Wang, J. Hao, Y. Su, F. Liu, J. An and J. Lian, *J. Mater. Chem. A*, 2016, **4**, 12929–12939.

44 X. Zhang, Y. Zhao and C. Xu, *Nanoscale*, 2014, **6**, 3638–3646.

45 S. Sahoo, R. Mondal, D. J. Late and C. S. Rout, *Microporous Mesoporous Mater.*, 2017, **244**, 101–108.

46 T. Zhu, H. B. Wu, Y. Wang, R. Xu and X. W. D. Lou, *Adv. Energy Mater.*, 2012, **2**, 1497–1502.

47 L. Qu, Y. Zhao, A. M. Khan, C. Han, K. M. Hercule, M. Yan, X. Liu, W. Chen, D. Wang, Z. Cai, W. Xu, K. Zhao, X. Zheng and L. Mai, *Nano Lett.*, 2015, **15**, 2037–2044.

48 C. Jiang, E. Hosono and H. Zhou, *Nano Today*, 2006, **1**, 28–33.

49 H. Sim, C. Jo, T. Yu, E. Lim, S. Yoon, J. H. Lee, J. Yoo, J. Lee and B. Lim, *Chemistry*, 2014, **20**, 14880–14884.

50 T. Chen, Y. Tang, Y. Qiao, Z. Liu, W. Guo, J. Song, S. Mu, S. Yu, Y. Zhao and F. Gao, *Sci. Rep.*, 2016, **6**, 23289.

51 T. Prasankumar, V. S. Irthaza Aazem, P. Raghavan, K. Prem Ananth, S. Biradar, R. Ilangovan and S. Jose, *J. Alloys Compd.*, 2017, **695**, 2835–2843.

52 Y. Jin, J. Xu, L. Wang, Q. Lu and F. Gao, *Chemistry*, 2016, **22**, 18859–18864.

53 Y. Tang, T. Chen, S. Yu, Y. Qiao, S. Mu, J. Hu and F. Gao, *J. Mater. Chem. A*, 2015, **3**, 12913–12919.

54 G. Zhang, M. Kong, Y. Yao, L. Long, M. Yan, X. Liao, G. Yin, Z. Huang, A. M. Asiri and X. Sun, *Nanotechnology*, 2017, **28**, 065402.

55 H. Quan, B. Cheng, D. Chen, X. Su, Y. Xiao and S. Lei, *Electrochim. Acta*, 2016, **210**, 557–566.

56 H. Chen, H. Ai, F. Liu, X. Chang, Y. Xue, Q. Huang, C. Wang, H. Lin and S. Han, *Electrochim. Acta*, 2016, **213**, 55–65.

57 H. Wang, J. Deng, Y. Chen, F. Xu, Z. Wei and Y. Wang, *Nano Res.*, 2016, **9**, 2672–2680.